RSC Advances

ROYAL SOCIETY OF CHEMISTRY

www.rsc.org/advances

Synthesis of mesoporous $NiCo_2O_4$-rGO by solvothermal method for charge storage applications

Ediga Umeshbabu,[a] G. Rajeshkhanna,[a] Ponniah Justin[b] and G. Ranga Rao[a*]

[a]Department of Chemistry, Indian Institute of Technology Madras, Chennai - 600036, India

[b]Department of Chemistry, Rajiv Gandhi University of Knowledge Technologies, RK Valley, Kadapa- 516330, Andhra Pradesh, India

Abstract

Spinel $NiCo_2O_4$ material has received considerable attention as an excellent supercapacitor material. In this study, we report facile and cost-effective solvothermal method for the synthesis of mesoporous $NiCo_2O_4$ anchored on reduced graphene oxide (rGO). The electrochemical activity of the $NiCo_2O_4$-rGO and pristine $NiCo_2O_4$ materials were evaluated by cyclic voltammetry (CV), chronopotentiometry (CP) and electrochemical impedance spectroscopy (EIS). The $NiCo_2O_4$-rGO composite electrode shows high specific capacitance value of 870 F g^{-1} at current density of 2 A g^{-1} and it retains 600 F g^{-1} capacitance even at high current density of 20 A g^{-1}. Pristine $NiCo_2O_4$ shows poor capacitance value of 315 F g^{-1} at 2 A g^{-1} and it retains only 191 F g^{-1} at 10 A g^{-1}. Further, $NiCo_2O_4$-rGO nanocomposite shows excellent cyclic performance with 90% capacitance retention even after 5000 charge-discharge cycles at high current density of 4 A g^{-1}, whereas pristine $NiCo_2O_4$ electrode shows only 45% capacitance retention. The high specific capacitance, remarkable rate capability and excellent cycling performance offered by $NiCo_2O_4$-rGO composite is attributed to the high surface area and high conductivity. In addition, rGO

*Corresponding author; Tel.: +91 44 2257 4226; Fax: +91 44 2257 4202; E-mail address: grrao@iitm.ac.in (G. Ranga Rao).

believed to shorten the diffusion, migration paths for electrolyte ions and an easy access of electrolyte ions into redox centers.

1. Introduction

Supercapacitors are energy storage devices. High power density, longer cycle life and quicker charging/discharging rates are important characteristics of supercapacitors which attracted tremendous attention in finding suitable materials and methods of synthesizing them .[1-3] Supercapacitors occupy the region between high energy density batteries and high power density dielectric capacitors in the Ragone plots.[4] Generally, supercapacitors store electrical energy by two types of charge storage mechanism: (i) non-Faradaic process and (ii) Faradaic/redox process. Carbon materials are well known for their charge storage by non-Faradaic processes, and also called electric double-layer capacitors.[1] On the other hand metal oxides are considered highly suitable for energy storage by Faradaic process and are pseudocapacitors.[5,6] Hitherto, numerous transition metal oxides such as RuO_2,[7] MnO_2,[8] NiO,[9] Co_3O_4,[10] Fe_2O_3,[11] V_2O_5,[12] MoO_3[13] and TiO_2[14] have been investigated for their pseudocapacitive behavior. Recently binary metal oxides such as $NiCo_2O_4$,[15-18] $NiMn_2O_4$,[19] $ZnCo_2O_4$,[20] $CoMn_2O_4$,[21] and $CuFe_2O_4$[22] have been preferred in foremost place than simple metal oxides because of variable oxidation states present, high electrical conductivity and lower activation energy for electron transfer between cations.[23] Among binary metal oxides, $NiCo_2O_4$ has turned out to be a promising material for supercapacitor electrodes due to its high theoretical capacitance ~3560 F g^{-1} and high electronic conductivity.[24,25] The electronic conductivity of $NiCo_2O_4$ is two times higher than the parent NiO and Co_3O_4.[15,16] But with increasing in demand for producing high rated supercapacitors, specific capacitance, rate capability and cyclic performance should commence first preference in achieving a secure market place. Thus, the spinel $NiCo_2O_4$ with the diverse morphologies has been synthesized

by hydrothermal, solvothermal, sol-gel, electrochemical deposition and microwave assisted methods.[17,18] However, spinel nickel cobaltite materials show limited cycling span due to pulverization induced by charge/discharge process. This can eventually lead to commercial limitations which should be addressed by controlling the volumetric change during charge/discharge processes. Encapsulation of nanostructured nickel cobaltite with graphene is thought to be the best way to enhance the capacitance and cyclic performance of $NiCo_2O_4$.[26-28]

Graphene is a 2D atomic sheet of sp^2-hybridized carbon atoms arranged in a hexagonal lattice. The planar sp^2-hybrid orbitals form σ-bonds in the honeycomb lattice and the remaining $2p_z$ orbitals on carbon atoms are delocalized in π symmetry orientation. The delocalized $2p_z$ electrons are largely responsible for high electronic conductivity of graphene. In addition to conductivity, graphene also has desirable characteristics such as high surface area (theoretical value of 2630 m^2 g^{-1}), good thermal/chemical stability and high structural flexibility.[29-31] Due to these unique properties, graphene is considered as a good blending material to prepare graphene based metal oxide hybrid nanocomposites for energy storage and conversion applications.[30-33] In electrochemical systems, graphene can be effective in improving specific capacitance, rate capability and cyclic permanence of the metal oxide-graphene hybrid nanocomposites by (i) controlling the nanocrystalline morphology of active materials, (ii) providing efficient electronic and ionic transport pathways, and (iii) improving the interfacial contact between active material and conductive graphene.

Recently, different $NiCo_2O_4$-graphene hybrid nanocomposites have been designed by different approaches and their performance tested for supercapacitors.[26, 34-39] For example, Wang et al. synthesised $NiCo_2O_4$-rGO composite using self-assembly method by exfoliating Ni-Co hydroxides and assembling with GO followed by heat treatment. These self-assembled 2D nanosheets of $NiCo_2O_4$-rGO composite exhibits higher specific capacitance of 835 F g^{-1}

at 1 A g^{-1}.[35] Shen et al. fabricated RGO-$NiCo_2O_4$ nanocomposite by hydrothermal approach using Poly (diallyldimethylammonium chloride) as an additive agent and obtained a specific capacitance of 671 F g^{-1} at 5 mV s^{-1}.[36] In another study, Wei et al. developed 3D mesoporous hybrid $NiCo_2O_4$@graphene nanoarchitectures by hydrothermal process using freeze dried grephene oxide and showed a maximum capacitance of 778 F g^{-1} at 1 A g^{-1}.[37] Wang et al. explored $NiCo_2O_4$ nanowires-loaded rGO composite synthesized by facile hydrothermal method using hexamethylenetetramine as a structure directing agent and exhibited a higher specific capacitance of 737 F g^{-1} at 1 A g^{-1}.[38] Microwave irradiation followed by mild heating has been adopted by Del Monte et al. to synthesize $NiCo_2O_4$-GO nanocomposite. This material contains $NiCo_2O_4$ nanoparticles embedded in the GO composite and showed higher specific capacitance value of 925 F g^{-1} at 1.5 A g^{-1}.[39] However, the synthesis methods discussed so far are complex and time-consuming. In addition, there is a possibility of restacking rGO or graphene sheets which can affect the electrochemical performance of the hybrid nanocomposites. There is scope to improve the morphology of $NiCo_2O_4$-rGO with uniform particle size and high surface area, while avoiding the aggregation of GO.

Here we report an efficient two step strategy to synthesize mesoporous $NiCo_2O_4$-rGO ultrathin nanosheets under solvothermal conditions in the presence of polymeric surfactant, polyvinylpyrrolidone (PVP). $NiCo_2O_4$-rGO ultrathin nanosheets are obtained by controlling the nucleation and growth of NiCo-glycolate nanosheets on the surface of rGO followed by thermal treatment. Reduced graphene oxide (rGO) acts as conductive support in this material and improves the electrochemical performance. The role of PVP is to control the size of $NiCo_2O_4$ particles and prevent the aggregation of GO.[22,40,41] The obtained mesoporous $NiCo_2O_4$-rGO ultrathin nanosheets show high specific capacitance, remarkable rate capability and good cycling performance during charge-discharge process.

2. Experimental Section

2.1 Synthesis of GO and $NiCo_2O_4$-rGO composite

Graphene oxide (GO) was synthesized from graphite powder by a modified Hummers method.[42] In this method, 34.5 mL of concentrated H_2SO_4 was added to a mixture of 1.5 g of graphite powder and 0.75 g of $NaNO_3$, and the resulting mixture was cooled to 0 °C using an ice bath. 4.5 g solid $KMnO_4$ was added slowly while keeping the reaction temperature below 20 °C. After the addition of $KMnO_4$, the reaction was carried out at 35 °C for 7 h under magnetic stirring. Additional 4.5 g $KMnO_4$ was added and continued stirring for 12 h at 35 °C. The reaction mixture was then cooled to room temperature and poured into 200 mL of ice water and 1.5 mL 30% H_2O_2 added. The mixture was finally centrifuged, washed several times with water, 30% HCl and ethanol. The product obtained was dispersed in water, kept for 30 min sonication, filtered and finally vacuum-dried overnight at 60 °C.

100 mg of as synthesized GO was dispersed in 100 mL of ethylene glycol (EG). After sonication for 15 min, 50 mg of PVP (weight-averaged molecular weight, M_w = 40000 g mol^{-1}) was added and then stirred for 1 h. 1 g of $Ni(CH_3COOH)_2.4H_2O$ and 2 g of $Co(CH_3COOH)_2.4H_2O$ were added to the above solution and continued stirring for 3 h to get complete homogeneity. The homogeneous mixture was transferred to Teflon lined stainless steel autoclave and kept it in electrical oven at 180 °C for 12 h. The autoclave was then allowed to cool to room temperature, and resulting precipitate was separated by centrifugation, washed with excess ethanol and water, and then dried in oven at 60 °C for 12 h. The dried solid sample was calcined in air at 350 °C for 3 h. Pristine $NiCo_2O_4$ was prepared by the same method without adding GO. The NiCo-glycolate-rGO and NiCo-glycolate precursor samples after calcined were denoted as $NiCo_2O_4$-rGO and $NiCo_2O_4$ respectively.

.

2.2 Materials characterization

Thermogravimetric analyses (TGA) of samples were performed on TA make TGA Q500V20.10 Build 36 instrument, in air flow and with linear heating rate of 20 °C per min, from room temperature to 800 °C. The powder X-ray diffraction (XRD) patterns were obtained using Bruker AXS D8 advanced diffractometer at room temperature using Cu Kα (λ = 0.15406 nm) radiation generated at 40 kV and 30mA with scan rate of 0.02° per min from 5 to 80°. Raman analysis of the resulting samples was carried out on Horiba HR 800UV confocal Raman spectrometer with λ = 632.8 nm and He-Ne laser as the excitation source. Fourier transform infrared (FT-IR) spectra were recorded using JASCO FT-IR-4100 spectrophotometer by KBr pellet method at room temperature. X-ray photoelectron spectroscopy (XPS) measurements were conducted using an Omicron ESCA Probe spectrometer employing Mg Kα (hν = 1253.6 eV) as the ionization source. The C 1s at 284.5 eV has been used as a reference binding energy. Nitrogen adsorption and desorption experiments were carried out by Micromeritics ASAP 2020 analyzer. The samples were outgassed at 200 °C for 12 h in a dynamic vacuum before physisorption measurements. The specific surface area was calculated using Brunauer- Emmet-Teller (BET) method, and pore size distribution of the samples was obtained from Barret-Joyner-Halenda (BJH) method. Surface morphologies of calcined products were characterized by field emission scanning electron microscope (SEM, FEI, Quanta 400), the powder samples deposited on conducting carbon tape before mounting on the microscope sample holder for analysis. High-resolution transmission electron microscopy (HR-TEM) images were obtained using JEOL JEM-3010 machine operated at 200 kV.

2.3 Electrochemical measurements

The working electrode for evaluating the electrochemical properties of resulting active material was fabricated by mixing 80 wt% of $NiCo_2O_4$-rGO (or $NiCo_2O_4$) sample with 10

wt% acetylene black in an agate mortar. To this mixture 10 wt% of polyvinylidenedifluoride (PVDF) binder with a few drops of 1-methyle 2-pyrrolydone (NMP) were added to form slurry. The slurry was coated (area of coating = 1cm^2) on a pretreated battery-grade polished Ni foil (0.2 mm thick) and dried at 60 °C for 10 h. The approximate mass of an active material on each electrode was 1mg cm^{-2}. Cyclicvoltammetry (CV), chronopotentiometry (CP) and electrochemical impedance spectroscopy (EIS) studies were performed using CHI6081C electrochemical work station in a three electrode system. Before electrochemical studies 30 CV cycles were performed in 2 M KOH to activate the working electrode. $NiCo_2O_4$-rGO (or $NiCo_2O_4$) sample coated on Ni foil, Pt foil (1 x 2 cm^2) and Hg/HgO (1.0 M KOH) were used as working, counter and reference electrodes. All the experiments were performed using freshly prepared aqueous 2 M KOH as electrolyte.

3. Results and discussion

3.1 Morphology and structure of the material

A plausible formation mechanism of the mesoporous ultrathin nanosheets of $NiCo_2O_4$-rGO composite is shown in scheme 1. In the whole process, several reactions could take place as follows: first, GO was dispersed in ethylene glycol containing PVP surfactant. The hydrophilic oxygen functional groups such as hydroxyl, epoxy, carbonyl, and carboxyl groups on the surface of GO provides good anchoring sites for positively charged Co^{2+} and Ni^{2+} ions through electrostatic forces. Under solvothermal conditions at 180 °C, NiCo-glycolate nanosheets were formed on the surface of rGO sheets through nucleation, aggregative growth process and oriented attachment mechanism. During these processes several factors like van der Waals forces, hydrogen bonding, hydrophobic attraction, crystal field attraction, electrostatic and dipolar fields, intrinsic crystal contraction and Ostwald ripening would be contributed.[15,43] During this process GO was also reduced into reduced

graphene oxide (rGO) by ethylene glycol and solvothermal conditions. After thermal treatment in air the NiCo-glycolate-rGO precursor transformed into porous $NiCo_2O_4$-rGO nanosheets.

The powder XRD pattern of uncalcined NiCo-glycolate-rGO precursor is shown in Fig. S1, A strong diffraction peak at 10.8° is characteristic of metal glycolate (NiCo-glycolate).[44-46] The thermal decomposition behavior of GO, NiCo-glycolate-rGO and NiCo-glycolate precursor samples was determined by TGA analysis as shown in Fig. S2 and 1A. For GO, there are three step weight losses (Fig. S2), the first weight loss observed below 100 °C is due to the elimination of physisorbed water molecules. The second weight loss observed at 218 °C is ascribed to the removal of oxygen functional groups on the surface of GO. The third weight loss observed at 570 °C corresponds to the combustion of carbon skeleton of GO or rGO. For the precursor samples (Fig. 1A), a small weigh loss below 150 °C is attributed to the removal of adsorbed moisture while second weight loss observed between 200 °C to 350 °C corresponds to the decomposition of NiCo-glycolate-rGO/NiCo-glycolate precursors into $NiCo_2O_4$-rGO/$NiCo_2O_4$. The weight loss observed above 800 °C is ascribed to the complete decomposition of spinel $NiCo_2O_4$ structure.[15] Further, the content of $NiCo_2O_4$ in the $NiCo_2O_4$-rGO composite is estimated to be 88.8% and rGO content is 12.2%. The powder XRD patterns of the GO, $NiCo_2O_4$-rGO and $NiCo_2O_4$ samples are shown in Fig. 1B. For GO, the diffraction peak at 2θ value of 10.5° observed is due to (002) plane of graphitic oxide with interplanar spacing of 0.84 nm. The presence of oxygen containing functional groups on the surface of GO increases the interplanar spacing from 0.34 nm for graphite to 0.84 nm for GO. Further, both $NiCo_2O_4$-rGO and $NiCo_2O_4$ samples show the reflections (shown in Fig. 1B) corresponding to face centered cubic spinel structure of $NiCo_2O_4$ (JCPDS card no: 73-1702) with space group of Fd3m (227). In both samples, no other impurity peaks of the $NiCo_2O_4$ were sensed, suggesting a complete conservation to $NiCo_2O_4$ without any impurity.

In $NiCo_2O_4$-rGO composite, the reflection for GO or rGO is not observed, which may be due to insufficient carbon content in the composite.[38,47]

These samples are further analyzed by Raman and FT-IR to confirm the presence of rGO in the composite. Fig. 2A shows Raman spectra of GO, $NiCo_2O_4$-rGO and $NiCo_2O_4$ samples. Both GO and $NiCo_2O_4$-rGO composite samples show two broad peaks at about 1330 cm^{-1} (D-band) and 1583 cm^{-1} (G-band). The G-band corresponding to an E_{2g} mode of graphite is associated to the vibration of sp^2 bonded carbon atoms in a 2-D hexagonal lattice, whereas D-band is ascribed to the defects and disorders in the hexagonal graphitic carbon layers.[29,30,34] In the Raman spectra of $NiCo_2O_4$-rGO and pristine $NiCo_2O_4$ samples, peaks observed at around 181, 456, 501 and 654 cm^{-1} could be attributed to F_{2g}, E_g, F_{2g}, and A_{1g} of the phonon modes of $NiCo_2O_4$, which are related to the vibrations of Co–O and Ni–O bonds.[48] Fig. 2B shows FT-IR spectra of GO, $NiCo_2O_4$-rGO and $NiCo_2O_4$ samples. The characteristic oxygenated functional groups of GO like C=O (~1728 cm^{-1}) and C–OH (1398 cm^{-1}) carboxylic groups, C–O–C (~1051 cm^{-1}) epoxy groups, and O–H (~3400 cm^{-1}) are observed in FT-IR spectra of GO. In addition, an absorption band at ~1623 cm^{-1} due to the skeletal C=C vibration of unoxidized graphitic domains is evident. Except the C=C skeletal vibration, all other oxygenated functional groups greatly diminished or extinct in $NiCo_2O_4$-rGO composite indicating the reduction of GO into reduced graphene oxide (rGO) by ethylene glycol under solvothermal conditions. In the FT-IR spectra of $NiCo_2O_4$-rGO composite and pristine $NiCo_2O_4$ samples observed two strong peaks at lower frequencies (553 and 641 cm^{-1}) can be assigned the stretching vibrations of the Ni-O and Co-O bonds in nickel cobalt oxide.[38]

The $NiCo_2O_4$-rGO composite is analyzed by photoemission spectroscopy to identify the chemical species which may contribute to the capacitive performance. Fig. S3 shows the X-ray photoelectron survey spectrum of the composite. It shows the photoemission signatures of Ni, Co, O and C. The deconvoluted spectral regions of C 1s, O 1s Co 2p and Ni 2p of

$NiCo_2O_4$-rGO composite are presented in Fig. 3. The C 1s region in Fig. 3A shows peaks at 287.9, 286.0 and 284.5 eV corresponding to oxygenated carbon species (C=O), C–OH, and C=C/C–C, respectively.[36,50] Accordingly the O 1s region in Fig. 3B shows three components at 529.7, 531.3, and 533 eV which are generally attributed to oxygen bonded to Ni and Co (Ni-O-Co),[36] defect sites with minimum oxygen coordination or oxygenated carbon species, and O-H groups on the sample surface, respectively.[34,50] The Co 2p spectrum in Fig. 3C consists of spin-orbit doublets and related satellite features characteristic of Co^{2+} and Co^{3+} ions.[50] The Ni 2p spectrum also shows the spin-orbit doublets due to Ni^{2+} and Ni^{3+} ions along with intense shakeup satellites in Fig. 3D.[34] Based on the percentage calculations, the sample contains higher amounts of Co^{3+} and Ni^{3+} ions than Co^{2+} and Ni^{2+} ions. The higher oxidation states are expected to facilitate fast charge transport across the electrode/electrolyte interface. These results show that the surface of $NiCo_2O_4$-rGO composite contains $Co^{3+/2+}$ and $Ni^{3+/2+}$ couples synergetic to each other and contribute to charge storage processes.[34,36,50]

The surface morphologies of the samples are analyzed by FESEM. The images of GO in Fig. S4 show typical homogeneous wrinkled flake-like morphology of very thin GO sheets. The morphology of $NiCo_2O_4$-rGO composite, however, resembles porous ultrathin nanosheets (Fig. 4A to 4C), which resulted from the thermal decomposition of NiCo-glycolate-rGO precursor. Similarly, pristine $NiCo_2O_4$ also developed ultrathin porous nanosheets as shown in Fig. 4D to 4F. The composition of $NiCo_2O_4$-rGO composite is further verified by energy X-ray dispersive spectroscopy (EDS) analysis as shown in Fig. S5. The composite material contains Ni, Co, O, and C with Ni:Co ratio is virtually 1:2. The microstructural properties of $NiCo_2O_4$-rGO composite was further analyzed by TEM. Fig. 5A and 5B shows different magnification TEM images of GO. This clearly shows that GO sheet is very thin, flat and flexible, which conforms that the complete exfoliation of graphite oxide into few layered GO nanosheets. Fig. 5C and 5D shows the TEM images of $NiCo_2O_4$-rGO

composite. It clearly indicates that porous ultrathin nanosheets of $NiCo_2O_4$ grown on rGO sheets. And also nanosheets are made up by large number of interconnected $NiCo_2O_4$ nanoparticles with the uniform size. The interplanar spacing of 0.242 nm, 0.281 nm and 0.468 nm are shown in Fig. 5E, which are all well matched with (311), (220) and (111) planes of spinel $NiCo_2O_4$. The polycrystalline nature of $NiCo_2O_4$-rGO composite was confirmed by selected-area electron diffraction (SAED) patterns as shown in Fig. 5F. The SAED of $NiCo_2O_4$-rGO composite was composed of well-defined rings, the diffraction rings in the SAED patterns can be readily indexed to the planes of (111), (220), (311) (440) and (511) of spinel nickel cobaltite (JCPDS card no. 73-1702).

The pseudocapacitive performance of an electrode material is closely related to the distribution of the pore size and specific surface area of the electroactive material.[9,10] The BET specific surface area and porosity of GO, $NiCo_2O_4$-rGO and $NiCo_2O_4$ samples are determined by N_2 adsorption-desorption isotherms at 77 K using N_2 as an adsorbent. Fig. 6 shows BET isotherms of $NiCo_2O_4$-rGO and $NiCo_2O_4$ samples, which characterize "type IV" isotherms with H3 hysteresis loops indicating the mesoporous nature of the respective samples. Inset of Fig. 6 shows the BJH pore size distribution plots for $NiCo_2O_4$-rGO and $NiCo_2O_4$ samples. The average pore diameters of these samples are found to be in mesoporous region, with tri-modal pore size distribution for $NiCo_2O_4$-rGO and bi-modal for $NiCo_2O_4$. However, the pore size distribution maxima are centered at 1.7, 4.5 and 22 nm for $NiCo_2O_4$-rGO composite, whereas those in pristine $NiCo_2O_4$sample at 1.7 nm and 15 nm. The BET specific surface area for $NiCo_2O_4$-rGO composite and pristine $NiCo_2O_4$ samples are 84 m^2/g and 48 m^2/g. However, the modified Hummers method route obtained GO nanostructure specific surface area shows 96 m^2/g (Fig. S6), this is relatively higher than the $NiCo_2O_4$-rGO composite. The decreased surface area in the $NiCo_2O_4$-rGO composite is due to the preferential blocking of the pores by the large size nanocrystalline $NiCo_2O_4$. Further, the

electrical conductivity of resulting $NiCo_2O_4$-rGO and pristine $NiCo_2O_4$ materials was measured by four-point probe method and estimated to be 5.23 s/m for $NiCo_2O_4$-rGO, and 1.21 s/m for pristine $NiCo_2O_4$. The high surface area and electrical conductivity of $NiCo_2O_4$-rGO nanocomposite may facilitate better transport of electrolyte ions through nanochannels and for efficient redox reactions during charge-discharge processes.

3.2 Electrochemical studies

The pseudocapacitive behavior of the resulting electroactive materials were tested by CV and CP tests. The CV curves of both $NiCo_2O_4$-rGO and pristine $NiCo_2O_4$ electrodes at different scan rates in the potential range of 0.0 to 0.55V (vs. Hg/HgO) are displayed in Fig. 7A and 7B. The CV curves of $NiCo_2O_4$-rGO and pristine $NiCo_2O_4$ electrodes clearly show unsymmetrical pattern with respect to different scan rates indicating kinetic irreversibility in the redox process due to polarization and ohmic resistance during the faradaic reactions.[15] The CV curves of GO in Fig. S7A are rectangular in shape which are typical of electric double layer capacitive behavior. However, in $NiCo_2O_4$-rGO composite, each CV curve shows two pairs of redox current peaks associated to the reversible reactions of $Co^{2+} \rightleftarrows Co^{3+}$ and $Ni^{2+} \rightleftarrows Ni^{3+}$ couples. The CV curves of $NiCo_2O_4$-rGO sample are distinctly different from those of pristine $NiCo_2O_4$ where $Co^{2+} \rightleftarrows Co^{3+}$ redox features can be seen clearly and $Ni^{2+} \rightleftarrows Ni^{3+}$ redox features are elusive.[15,16] The two pairs of strong redox peaks in $NiCo_2O_4$-rGO composite as a result of strong chemical interactions between the nanoscale $NiCo_2O_4$ particles and the residual oxygen-containing functional groups on surface of the rGO or van der Waals interactions between $NiCo_2O_4$ and rGO.[34,35] The intimate chemical interactions between $NiCo_2O_4$ and rGO promote fast electron transport and results in strong redox features of both $Co^{2+} \rightleftarrows Co^{3+}$ and $Ni^{2+} \rightleftarrows Ni^{3+}$ in $NiCo_2O_4$-rGO.[35,49] It is also important to note that the CV curves of $NiCo_2O_4$-rGO composite electrode

show much larger integrated areas and specific current than those of pristine $NiCo_2O_4$ electrode (compare Fig. 7A and 7B). This suggests that $NiCo_2O_4$-rGO has higher electrochemical activity and faster activation process. This is due to high surface area, electrical conductivity and high flexibility of graphene (rGO) present in the composite. In addition, rGO prevents the aggregation of nickel cobalt oxide particles and promotes effective redox reactions at the electrode-electrolyte interface. We have further ensured that the capacitance contribution of Ni foil is negligible to the total capacitance of pristine $NiCo_2O_4$ or $NiCo_2O_4$-rGO electrodes (see Fig. S8). Further, with increasing scan rates in Fig. 7A and 7B, peak currents are found to increase, and the potentials of anodic and cathodic peaks shift to positive and negative directions, respectively. This can be endorsed to strengthened electric polarization and reversibility reactions at higher scan rates. Because the reaction is limited by the ion diffusion rate, it is not going to satisfy the electronic neutralization during the reactions.

Trasatti analysis has been employed to evaluate the electrochemical charge storage properties of $NiCo_2O_4$-rGO and $NiCo_2O_4$ electrodes.[51-53] In this analysis, the total voltammetric charge (q_t) can be divided into two parts: (i) outer surface charge (q_o) or more accessible surface charge, and (ii) inner surface charge (q_i) or less accessible surface charge. The total charge exchanged between electrode and electrolyte, including both inner and outer charge storage as: $q_t = q_i + q_o$. The inner surface charge is a diffusion controlled reaction process, which mainly originates from the less accessible surface such as pores, grain boundaries, crevices and cracks. The outer surface charges, q_o storage is assumed to be not dependent on scan rates, it mainly initiated from the direct accessible surface, which corresponds to the region touching the electrolyte solution directly. In this case the reactive species diffusion does not control the reaction. Thus, the relationship of charge stored with

scan rate is given as: $q_t = q_o + k\nu^{-1/2}$, where ν is scan rate and k is a constant. The outer surface charge, q_o can be derived from the extrapolation of voltammetric charge, q as ν = ∞ from the plot of q *vs.* $\nu^{-1/2}$ (Fig. 7C), and the total charge (q_t) can be calculated from an extrapolation of voltammetric charge q at ν = 0 from the plot of $q^{-1/2}$ *vs.* $\nu^{1/2}$ (Fig. 7D). Then the inner charge q_i can be calculated from the subtraction of q_t and q_o. The estimated outer and inner surface charges of the two samples are displayed in Fig. 8. Further, the ratio of q_o/q_t for $NiCo_2O_4$-rGO composite and pristine $NiCo_2O_4$ electrodes are about 0.81 and 0.74, respectively. The higher ratio of q_o/q_t for $NiCo_2O_4$-rGO electrode indicates that a large proportion of charge is located at easily accessible sites which are easily accessible with minimum diffusion limitations. This can impart high-rate capability to $NiCo_2O_4$-rGO electrode.

Fig. 9A and 9B show galvanostatic charge-discharge (GCD) curves for $NiCo_2O_4$-rGO and $NiCo_2O_4$ electrodes at different current densities in the potential range between 0.05 to 0.55 V (vs. Hg/HgO). The nonlinearity in the charge-discharge curves indicates pseudocapacitance behavior owing to Faradaic reactions occurring at the electrode/electrolyte interface. This is in contrast with the electric double layer electrode materials like GO which typically shows linear behavior (Fig. S7B). Under similar current density conditions, $NiCo_2O_4$-rGO electrode exhibits longer discharge time than GO and $NiCo_2O_4$ electrodes (Fig. S9). Therefore, $NiCo_2O_4$-rGO electrode shows superior charge storage performance and high specific capacitance than pristine $NiCo_2O_4$ electrode. The specific capacitance (C_S, F g^{-1}) of the resulting electrodes was calculated from the discharge curves at different current densities by using the following equation:[35,54]

$$C_S = \frac{I \times \Delta t}{m \times \Delta V}$$

where, I is the applied current (A), m is the mass of active material (g), Δt is the discharge time (s) and ΔV is the discharge voltage (V). The specific capacitance values calculated for both electrodes at different current densities are shown in Fig. 9C. In both the electrodes the specific capacitance gradually decreases with increasing current density. At lower current densities voltage drop is negligible, and both outer and inner surface pores can be effectively utilized for electrolyte propagation and redox reactions, which can help to achieve high specific capacitance. Therefore, $NiCo_2O_4$-rGO composite exhibits high specific capacitance of 870 F g^{-1} while $NiCo_2O_4$ and GO electrode materials show only 315 and 54 F g^{-1} at current density of 2 A g^{-1}. $NiCo_2O_4$-rGO composite prepared in this work exhibited higher specific capacitance value than the values reported for similar $NiCo_2O_4$-rGO composites.[35-38] Furthermore, the $NiCo_2O_4$-rGO composite electrode maintains good specific capacitance value of 600 F g^{-1} (69% retention) even at higher current density of 20 A g^{-1} whereas, pristine $NiCo_2O_4$ shows about 61% capacitance retention even at 10 A g^{-1}.

Cycle life of supercapacitor is one of the most important parameter for the practical applications. Fig. 9D shows a cyclic life test for $NiCo_2O_4$-rGO and pristine $NiCo_2O_4$ electrodes at a current density of 4 A g^{-1}. $NiCo_2O_4$-rGO composite electrode shows excellent cyclic stability with 90% capacitance retention over 5000 long term charge-discharge cycles. This is significantly better than the cyclic performance of reported $NiCo_2O_4$-rGO composites listed in Table 1. Overall, $NiCo_2O_4$-rGO composite electrode exhibits high specific capacitance, rate capability and superior cyclic performance. Such good performance can be attributed to (i) the presence of rGO in the $NiCo_2O_4$-rGO hybrid structure enhances the effective specific surface area and shorten the diffusion, migration paths for electrolyte ions (ii) the intimate contact between rGO and $NiCo_2O_4$ promoting electrical conductivity, and

(iii) the rGO can effectively avoid the agglomeration of $NiCo_2O_4$ during charge-discharge process.[29,32,33]

The kinetics and charge transfer mechanism at an electrode/electrolyte interface of both the materials are studied by electrochemical impedance spectroscopy (EIS). Fig. S7C and Fig. 10A shows the Nyquist plots of GO, $NiCo_2O_4$-rGO and $NiCo_2O_4$ electrodes recorded in the frequency range of 10 mHz to 100 kHz at a bias potential of 0.3 V. The resulting impedance data is fitted by complex nonlinear least squares (CNLS) fitting method to the Randle equivalent circuit as shown in Fig. 10B. In this circuit, different parameters designate different electrochemical process occurring at an electrode/electrolyte interface. For both $NiCo_2O_4$-rGO and $NiCo_2O_4$ electrodes of the Nyquist plots were characterized by two distinct parts, a semi-circle loop at high-frequency and a linear line at low-frequency regions, suggesting different electrochemical phenomena during the electrochemical process on the electrode surface. At the high frequency region, the intersection with the real part (Z') represents the combined resistance as a result of ionic resistance of an electrolyte, intrinsic resistance of the substrate and contact resistance at the active material/current collector.[15] This value is almost same for both the electrode materials. However, the major difference is seen in the semicircles in which $NiCo_2O_4$-rGO electrode shows the semicircle with larger radius compared to pristine $NiCo_2O_4$ electrode. This shows that the resistance of $NiCo_2O_4$-rGO electrode is considerably less than that of $NiCo_2O_4$ electrode. The origin of this electrode resistance is the combination of the double layer capacitance (C_{dl}) on the oxide surface and ionic charge transfer resistance (R_{ict}) due to faradaic reactions. In the Nyquist plots the inclined portion of the curve at lower frequency is attributed to the Warburg impedance (Z_W) which is caused by the diffusion/transport of OH^- ions within the pores of $NiCo_2O_4$-rGO and $NiCo_2O_4$ electrodes during the redox reactions. The near vertical lines

along the imaginary axis (Z") in the lower frequency region indicate the capacitive behavior of the electrodes.

EIS provides complementary information about the frequency response of $NiCo_2O_4$-rGO and pristine $NiCo_2O_4$ electrode materials in supercapacitors and allows us to assess the capacitance changes with operating frequency. The complex form of the capacitance is dependent on frequency which can be defined as follows.[3]

$$C(\omega) = C'(\omega) + jC''(\omega)$$

where, C′ (ω) is the real part of the capacitance C (ω) which corresponds to the capacitance of the cell measured during the constant current discharge, and C" (ω) is the imaginary part of the capacitance C (ω) which is related to the losses in the form of energy dissipation. Further, the real C′ (ω) and imaginary C" (ω) parts of the capacitances can be defined as:

$$C'(\omega) = \frac{-Z''(\omega)}{\omega|Z(\omega)|^2} \quad \text{and} \quad C''(\omega) = \frac{-Z'(\omega)}{\omega|Z(\omega)|^2}$$

where, Z′ (ω) and Z" (ω) are the real and imaginary parts of the impedance Z (ω). The frequency dependent on real (C′) and imaginary (C″) components of the capacitance are shown in Fig. 10C and 10D. The capacitance (C′) declines with the increasing frequency (Fig. 10C). Both $NiCo_2O_4$-rGO and $NiCo_2O_4$ electrodes exhibits maximum capacitance at lower frequencies because electrolyte ions fully penetrate into the active material contributing to both inner and outer surface pores of the active material. At higher frequencies, electrolyte ions can have access only to outer surface pores of the active material and the contribution from inside pores is negligible resulting in decrease of the capacitance.[59] Further, the variation of the imaginary part of the capacitance (C″) with frequency is also shown in Fig.

10D. The maximum peak is associated with maximum capacitance (C″) at a frequency f_0 which can be used to calculate the relaxation time constant, $\tau = 1/2\pi f_0$.[50,60] The relaxation time constant is a measure of how fast the device can be charged and discharged reversibly. The calculated time constants for $NiCo_2O_4$-rGO and pristine $NiCo_2O_4$ electrodes are 300 ms and 425 ms respectively. The lower time constant for $NiCo_2O_4$-rGO indicates faster accessibility to electrolyte ions during the charge-discharge processes. This study clearly shows that $NiCo_2O_4$-rGO composite material is an excellent material for supercapacitor applications.

4. Conclusions

In summary, we have demonstrated a facile and cost effective solvothermal method to synthesis of $NiCo_2O_4$-rGO composite and pristine $NiCo_2O_4$ electrode materials by using PVP as surfactant/capping agent. The $NiCo_2O_4$-rGO composite electrode exhibits high specific capacitance of 870 F g^{-1} at current density of 2 A g^{-1} and good cyclic performance retaining 90% capacitance after 5000 charge-discharge cycles, whereas pristine $NiCo_2O_4$ electrode shows only 315 F g^{-1} specific capacitance with 45% capacitance retention. The high specific capacitance, good rate capability and excellent cycling ability of the $NiCo_2O_4$-rGO composite are attributed to reduced graphene oxide. In that, rGO enhances the surface area and conductivity of the composite. This enables more contact surface between active material and electrolyte ions during the charge-discharge process. In addition, shorten the diffusion, migration paths for electrolyte ions and an easy access of electrolyte ions into redox centers.

Supporting Information

Additional characterization data including the powder XRD pattern of uncalcined precursor, TGA ,BET, FESEM, CV CP and analysis of GO, XPS survey spectra and EDS spectrum of $NiCo_2O_4$-rGO nanocomposite, comparison of CV curves for Ni foil, pristine $NiCo_2O_4$ and

$NiCo_2O_4$-rGO, and comparison of CP curves for GO, $NiCo_2O_4$ and $NiCo_2O_4$-rGO are presented in the supporting information.

Acknowledgments

The authors gratefully acknowledge the financial support by MNRE 102/28/2006-NT and DRDO ERIP/ER/0600319/M/01/1052, New Delhi. The fellowships granted by CSIR to Umeshbabu and UGC to Rajeshkhanna are gratefully acknowledged.

References

1 L. L. Zhang and X. S. Zhao, *Chem. Soc. Rev.*, 2009, **38**, 2520–2531.

2 J. Yan, Q. Wang, T. Wei and Z. Fan, *Adv. Energy Mater.*, 2014, **4**, DOI: 10.1002/aenm.201300816J.

3 F. Beguin and E. Frackowiak, *Supercapacitors: Materials, Systems, and Applications*. Wiley–VCH: Weinheim, 2013.

4 Y. Gogotsi and P. Simon, *Science*, 2011, **334**, 917–918.

5 F. Shi, L. Li, X. L. Wang, C. D. Gu and J. P. Tu, *RSC Adv.*, 2014, **4**, 41910–41921.

6 J. Jiang, Y. Li, J. Liu, X. Huang, C. Z. Yuan and X. W. Lou, *Adv. Mater.*, 2012, **24**, 5166–5180.

7 P. Wang, H. Liu, Q. Tan and J. Yang, RSC Adv., 2014, **4**, 42839–42845.

8 W. Wei, X. Cui, W. Chen and D. G. Ivey, *Chem. Soc. Rev.*, 2011, **40**, 1697–1721.

9 P. Justin, S. K. Meher and G. Ranga Rao, *J. Phys. Chem. C*, 2010, **114**, 5203–5210.

10 S. K. Meher and G. Ranga Rao, *J. Phys. Chem. C*, 2010,**115**, 25543–25556.

11 S. Shivakumara, T. R. Penki and N. Munichandraiah, *J. Solid State Electrochem*, 2014, **18**, 1057–1066.

12 B. Saravanakumar, K. K. Purushothaman and G. Muralidharan, *ACS Appl. Mater. Interfaces*, 2012, **4**, 4484–4490.

13 Z. Cui, W. Yuan and C. M. Li, *J. Mater. Chem. A*, 2013, **1**, 12926–12931.

14 X. Lu, G. Wang, T. Zhai, M. Yu, J. Y. Gan, Y. Tong and Y. Li, *Nano Lett.*, 2012, **12**, 1690–1696.

15 E. Umeshbabu, G. Rajeshkhanna and G. Ranga Rao, *Int. J. Hydrogen Energy*, 2014, **39**, 15627–15638.

16 N. Garg, M. Basu and A. K. Ganguli, *J. Phys. Chem. C*, 2014, **118**, 17332–17341.

17 D. P. Dubal, P. Gomez-Romero,; B. R. Sankapal and R. Holze, Nano Energy, 2015, **11**, 377–399.

18 Z. Wu, Y. Zhu and X. Ji, *J. Mater. Chem. A*, 2014, **2**, 14759–14772.

19 M. Zhang, S. Guo, L. Zheng, G. Zhang, Z. Hao, L. Kang and Z. H. Liu, *Electrochim. Acta*, 2013, **87**, 546–553.

20 M. Davis, C. Gumeci, B. Black, C. Korzeniewski and H. W. Louisa, *RSC Adv*., 2012, **2**, 2061–2066.

21 Y. Xu, X. Wang, C. An, Y. Wang, L. F. Jiao, H. Yuan, *J. Mater. Chem. A*, 2014, **2**, 16480–16488.

22 M. Zhu, M. Meng, C. Wang and G. Diao, *ACS Appl. Mater. Interfaces*, **2013**, *5*, 6030–6037.

23 C. Yuan, B. H. Wu, Y. Xie and X. W. Lou, *Angew. Chem., Int. Ed.*, 2014, **53**, 1488–1504.

24 E. Mitchell, A. Jimenez, R. K. Gupta, B. K. Gupta, K. Ramasamy, M. Shahabuddin and S. R. Mishrad, *New J. Chem.*, 2015, **39**, 2181–2187.

25 Y. Li , Y. Zhang, Y. Li, Z. Wang, H. Fu, X. Zhang, Y. Chen, H. Z. Zhang and X. D Li, Electrochim. Acta, 2014, **145**, 177–184.

26 J. Xu, L. Li, P. Gao, L. Yu, Y. Chen, P. Yang, S. Gai and P. Yang, *Electrochim. Acta*, 2015, **166**, 206–214.

27 Y. J. Chen, J. Zhu, B. Qu, B. Lu, Z. Xu, *Nano Energy*, 2014, **3**, 88–94.

28 H. Wang, C. M. B. Holt, Z. Li, X. Tan, B. S. Amirkhiz, Z. Xu, B. C. Olsen, T. Stephenson and D. Mitlin, *Nano Res.*, 2012, **5**, 605–617.

29 W. Choi and J. W. Lee, *Graphene Synthesis and Applications*; Taylor Francis Group, 2012.

30 C. N. R. Rao, A. K. Sood, K. S. Subrahmanyam and A. Govindaraj, *Angew. Chem. Int. Ed.*, 2009, **48**, 7752 –7777.

31 X. Huang, Z. Y. Yin, S. Wu, X. Y. Qi, Q. He, Q. Zhang, Q. Yan, F. Boey and H. Zhang, *Small*, 2011, **7**, 1876–1902.

32 J. Hou, Y. Shao, M. W. Ellis, R. B. Moored and B. Yie, *Phys. Chem. Chem. Phys.*, 2011, **13**, 15384–15402.

33 Z. S. Wu, G. Zhou, L. C. Yin, W. Ren, F. Li and H. M. Cheng, *Nano Energy*, 2012, **1**, 107–131.

34 L. Wang, X. H. Wang, X. P. Xiao, F. G. Xu, Y. J. Sun and Z. Li, *Electrochim. Acta*, 2013**,** **111**, 937– 945.

35 H. W. Wang, Z. A. Hu, Y. Q. Y. L. Chang, Chen, H. Y. Wu, Z. Y. Zhang and Y. Y. Yang, *J. Mater. Chem.*, 2011, **21**, 10504–10511.

36 J. F. Shen, X. F. Li, N. Li and M. Ye, Electrochim. *Acta*, 2014, **141**, 126–133.

37 Y. Wei, S. Chen, D. Su, B. Sun, J. G. Zhu and G. Wang, *J. Mater. Chem. A*, 2014, **2**, 8103–8109.

38 G. He, L. Wang, H. Chen, X. Q. Sun and X. Wang, *Mater. Lett*., 2013, **98**, 164–167.

39 D. Carriazo, J. Patiño. M. C. Gutiérrez, M. L. Ferrer and F. Del Monte, *RSC Adv.*, 2013, **3**, 13690–13695.

40 L. Y. Pan, H. Zhao, W. Shen, X. Dong and J. Q. Xu, *J. Mater. Chem. A*, 2013, **1**, 7159–7166.

41 M. Cai, H. Qian, Z. Wei, J. Chen, M. Zheng and Q. F. Dong, *RSC Adv.*, 2014, **4**, 6379–6382.

42 D. C. Marcano, D. V. Kosynkin, J. M. Berlin, A. Sinitskii, Z. Z. Sun, A. Slesarev, L. B. Alemany, W. Lu and J. M. Tour, *ACS Nano*, 2010, **4**, 4806–4814.

43 G. Zhang, B. Y. Xia, X. Wang and X. W. Lou, *Adv. Mater.*, 2014, **26**, 2408–2412.

44 X. Wang, X. L. Wu, Y. G. Guo, Y. Zhong, X. Cao, Y. Ma and J. Yao, *Adv. Funct. Mater.*, 2010, **20**, 1680–1686.

45 X. Jiang, Y. Wang, T. Herricks and Y. Xia, *J. Mater. Chem.*, 2004, **14**, 695–703.

46 Y. Wang, X. Jiang and Y. Xia, *J. Am. Chem. Soc.,* 2003, **125**, 16176–16177.

47 D. T. Dam, X. Wang and J. M. Lee, *ACS Appl. Mater. Interfaces*, 2014, **6**, 8246–8256.

48 Z. -Q. Liu, K. Xiao, Q. -Z. Xu, N. Li, Y. -Z. Su, H. -J. Wang and S. Chen, *RSC Adv.*, 2013, **3**, 4372–4380.

49 Y. Luo, H. Zhang, D. Guo, J. Ma, Q. H. Li, L. Chen and T. H. Wang, *Electrochim. Acta*, 2014, **132**, 332–337.

50 P. Syedvali, G. Rajeshkhanna, E. Umeshbabu, G. U. Kiran, G. Ranga Rao and P. Justin, *RSC Adv.*, 2015, **5**, 38407–38416.

51 S. Ardizzone, G. Fregonara and S. Trasatti, *Electrochim. Acta*, 1990, **35**, 263–267.

52 X. Wang, W. S. Liu, X. Lu and P. S. Lee, *J. Mater. Chem*., 2012, **22**, 23114–23119.

53 C. Jo, I. Hwang, J. Lee, C. W. Lee and S. Yoon, *J. Phys. Chem. C*, 2011, **115**, 11880–11886.

54 C. Mondal, M. Ganguly, P. K. Manna, S. M. Yusuf and T. Pal, *Langmuir*, 2013, **29**, 9179–9187.

55 Q. Guan, J. Cheng, B. Wang, W. Ni, G. Gu, X. D. Li, L. Huang, G. C. Yang, F. Nie, *ACS Appl. Mater. Interfaces*, 2014, **6**, 7626–7632.

56 Y. Xu, J. Wei, L. Tan, J. Yua and Y. Chen, *J. Mater. Chem. A*, 2015, **3**, 7121–7131.

57 L. Ma, X. Shen, Z. Y. Ji, X. Cai, G. Zhu and K. Chen. *J. Colloid and Interface Sci*., 2015, **440**, 211–218.

58 W. W. Liu, C. Lu, K. Liang and B. K. A. Tay, *J. Mater. Chem. A*, 2014, **2**, 5100–5107.

59 M. Biswal, A. Banerjee, M. Deo and S. Ogale, *Energy Environ. Sci*., 2013, **6**, 1249–1259.

60 B. Fang and L. Binder, *J. Phys. Chem. B*, 2006**, 110***,* 7877–7882.

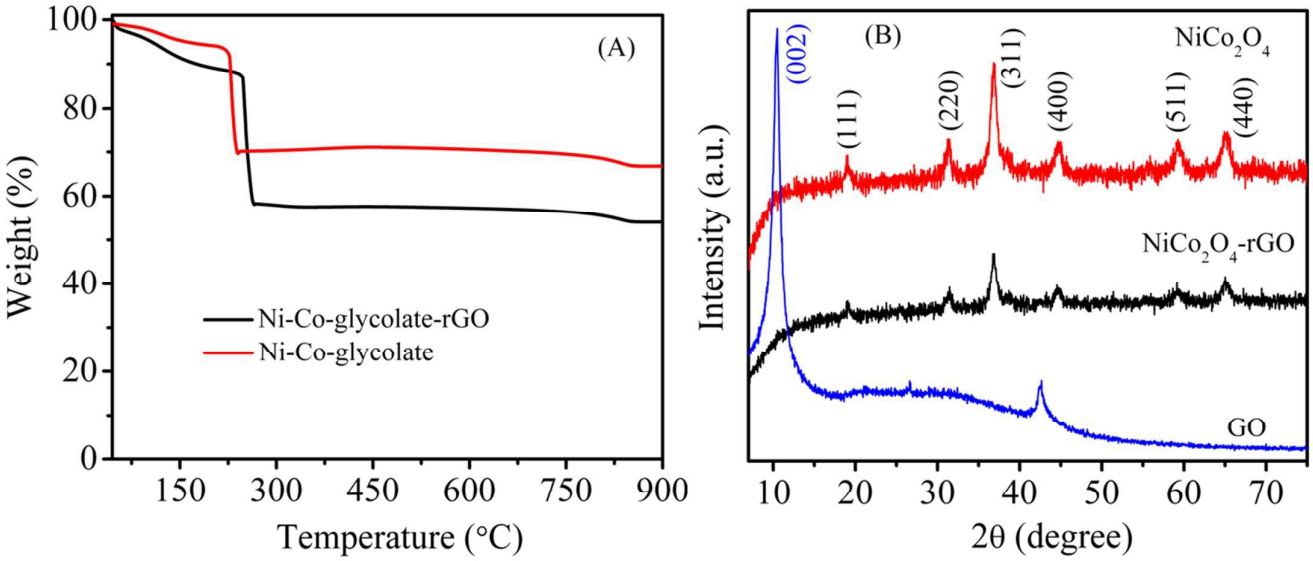

Fig. 1 (A) TGA curves of unclacined precursors (Ni-Co-glycolate-rGO and Ni-Co-glycolate); (B) PXRD patterns of GO, $NiCo_2O_4$-rGO and $NiCo_2O_4$ samples.

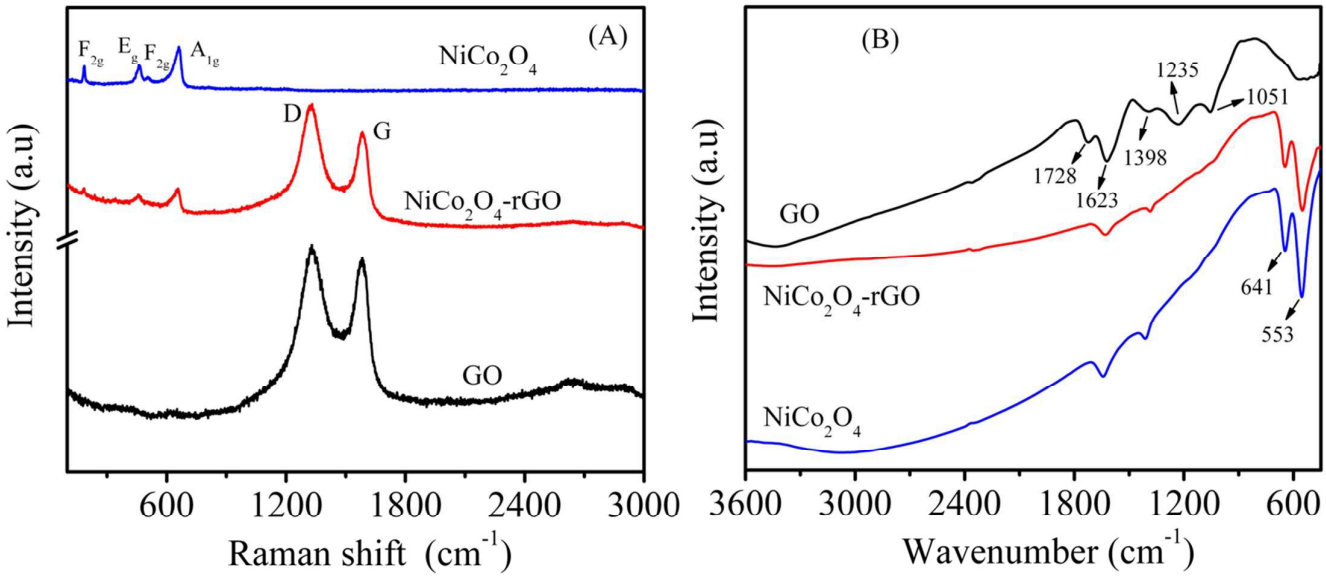

Fig. 2 (A) Raman spectra and (B) FTIR spectra of GO, $NiCo_2O_4$-rGO and $NiCo_2O_4$ samples.

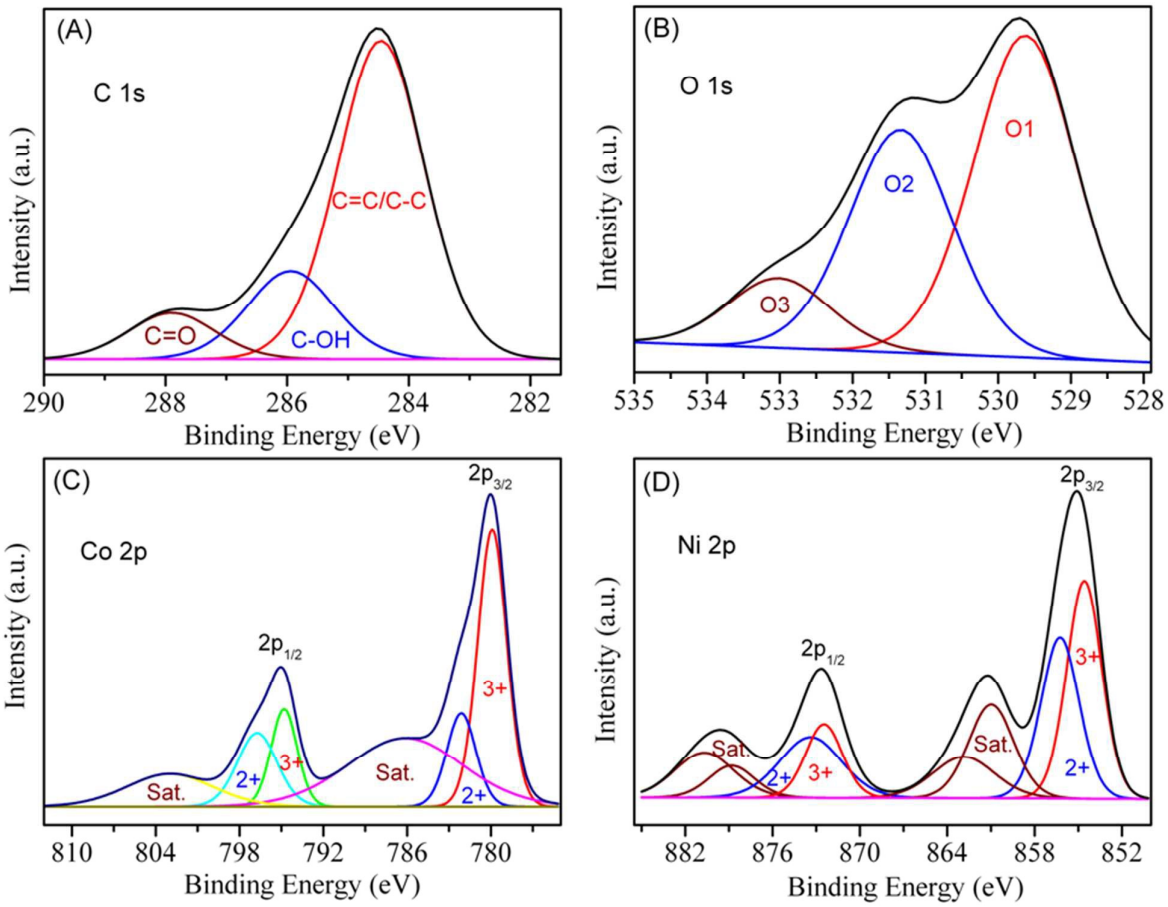

Fig. 3 Core level XPS spectra of (A) C 1s, (B) O 1s, (C) Co 2p and (D) Ni 2p for the $NiCo_2O_4$- rGO composite.

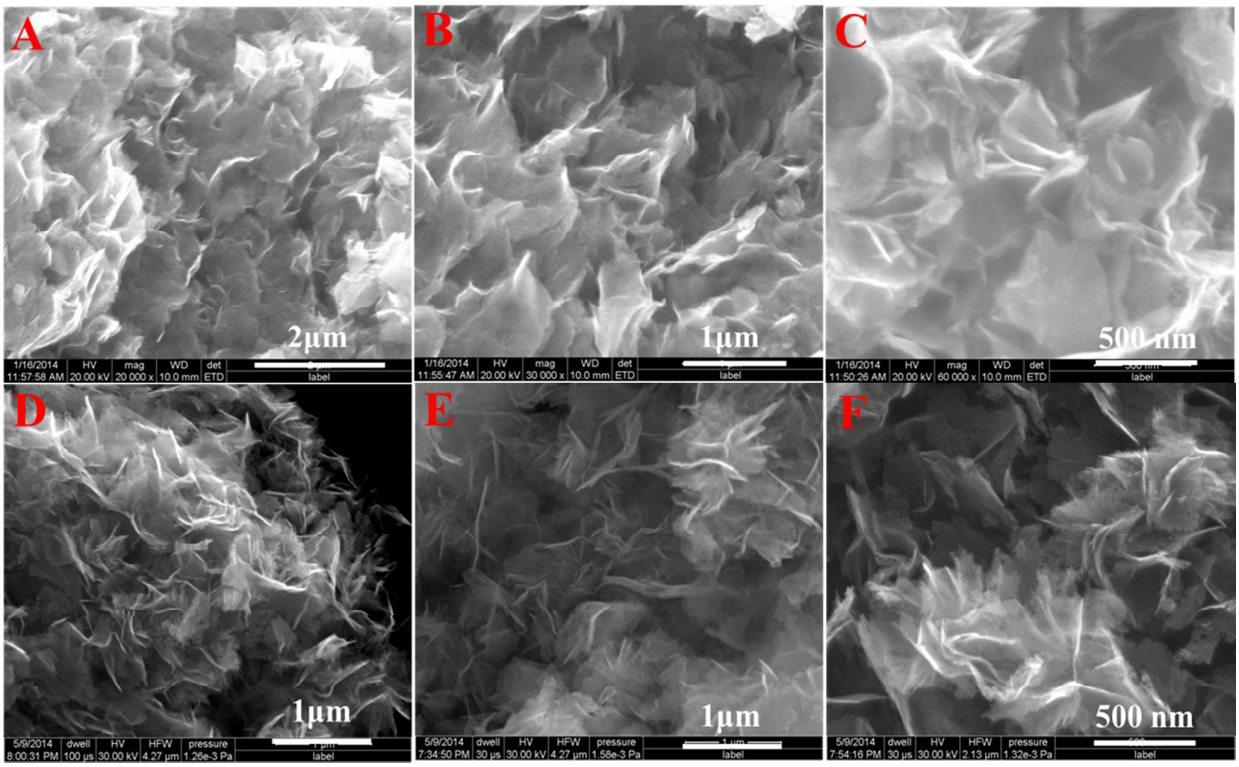

Fig. 4 Low- and high-resolution FESEM images of $NiCo_2O_4$-rGO (A to C) and $NiCo_2O_4$ (D to F) samples.

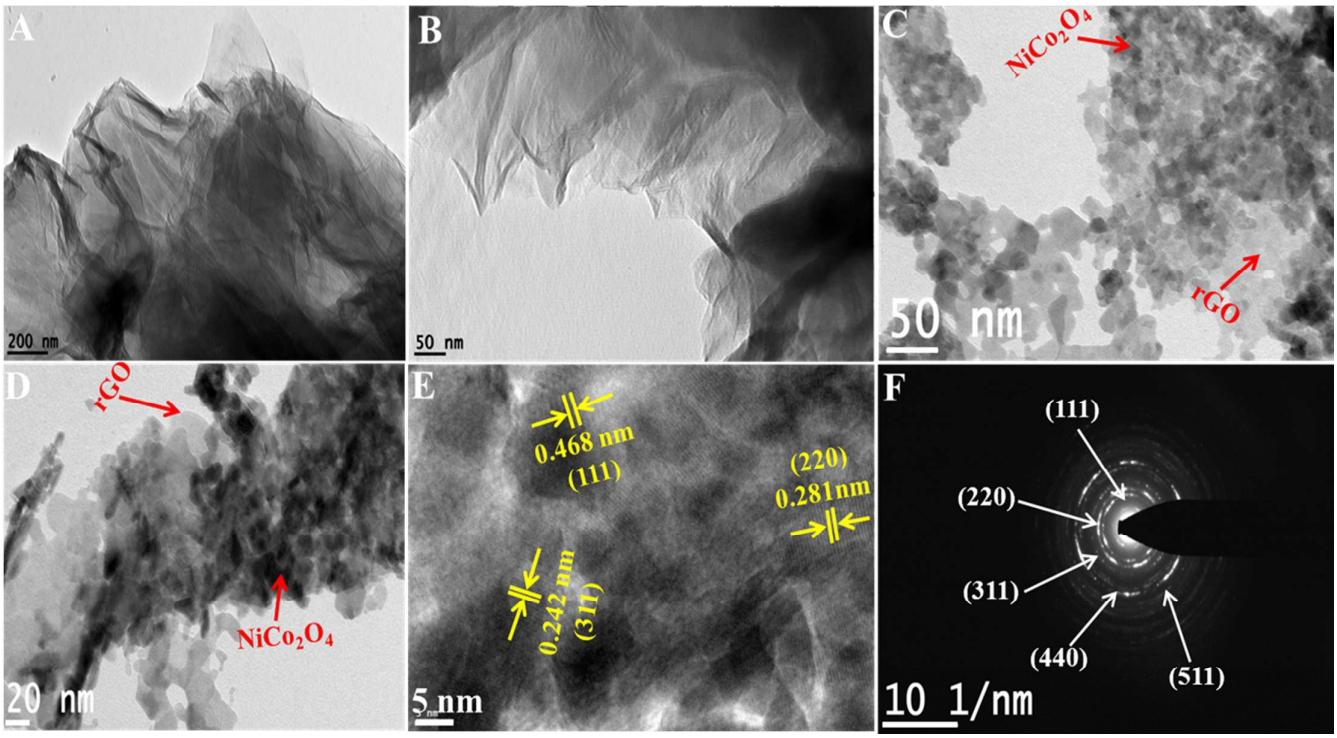

Fig. 5 TEM images of GO (A, B) and $NiCo_2O_4$-rGO (C to E) at different magnifications. (F) The SAED pattern for the $NiCo_2O_4$-rGO composite.

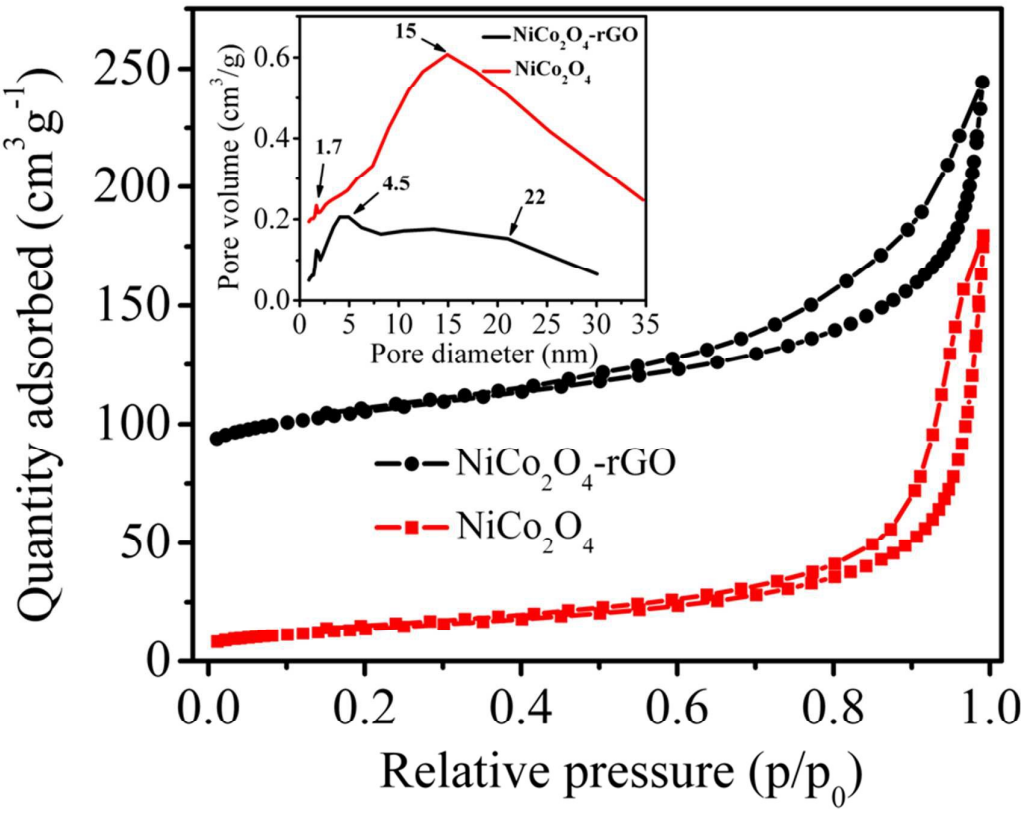

Fig. 6 N_2 adsorption–desorption isotherms of $NiCo_2O_4$-rGO and $NiCo_2O_4$ samples; inset shows corresponding BJH pore size distributions plots of $NiCo_2O_4$-rGO and $NiCo_2O_4$ samples.

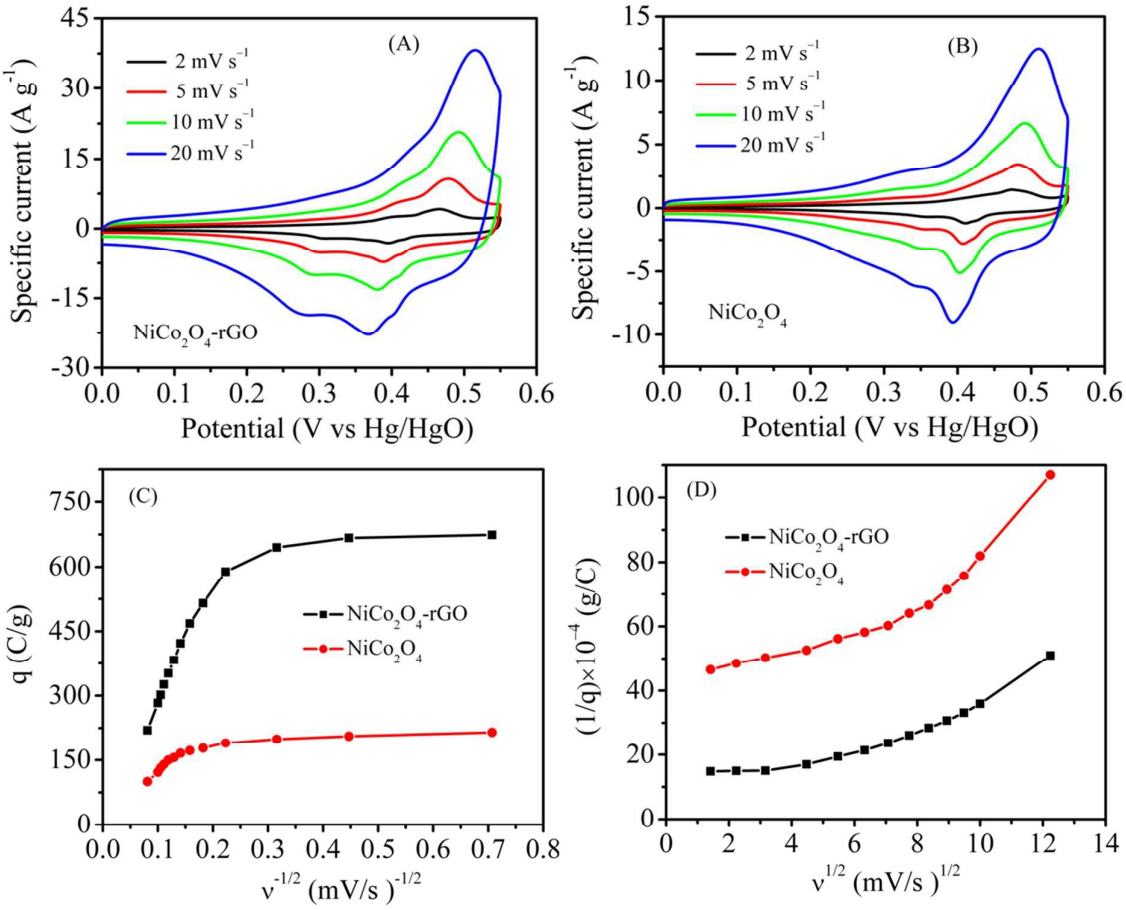

Fig. 7 Cyclic voltammograms of (A) $NiCo_2O_4$-rGO and (B) $NiCo_2O_4$ electrodes at different scan rates; Variation of the voltametric charge (q) against scan rates: (C) q vs. $\nu^{-1/2}$ and (D) 1/q vs. $\nu^{1/2}$ for the $NiCo_2O_4$-rGO and $NiCo_2O_4$ electrodes.

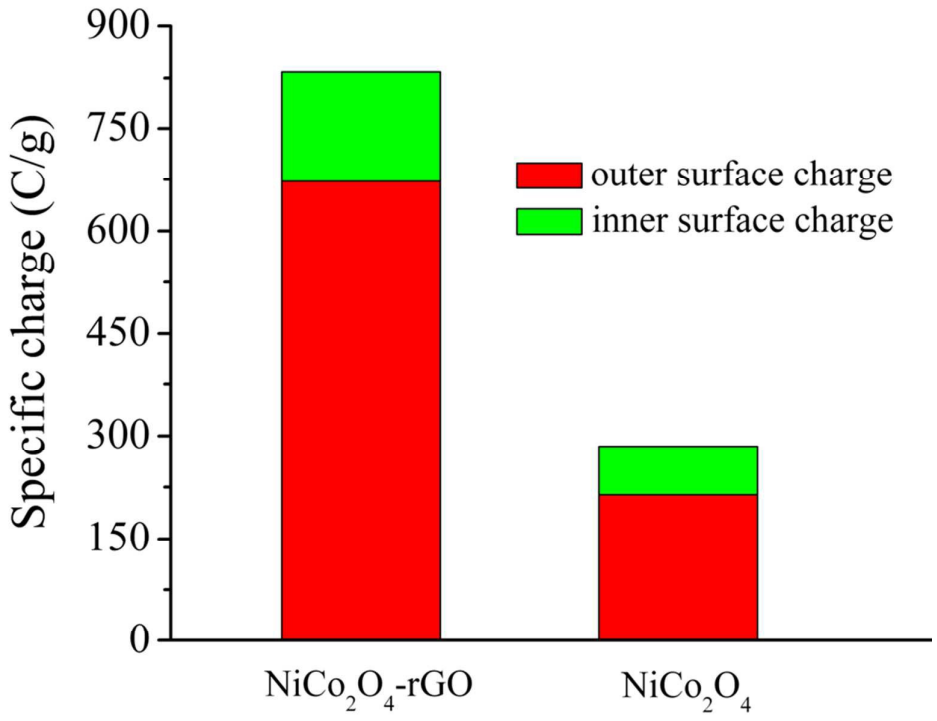

Fig. 8 Inner and outer surface charge storage profiles of $NiCo_2O_4$-rGO and $NiCo_2O_4$ electrodes, obtained from cyclic voltammograms.

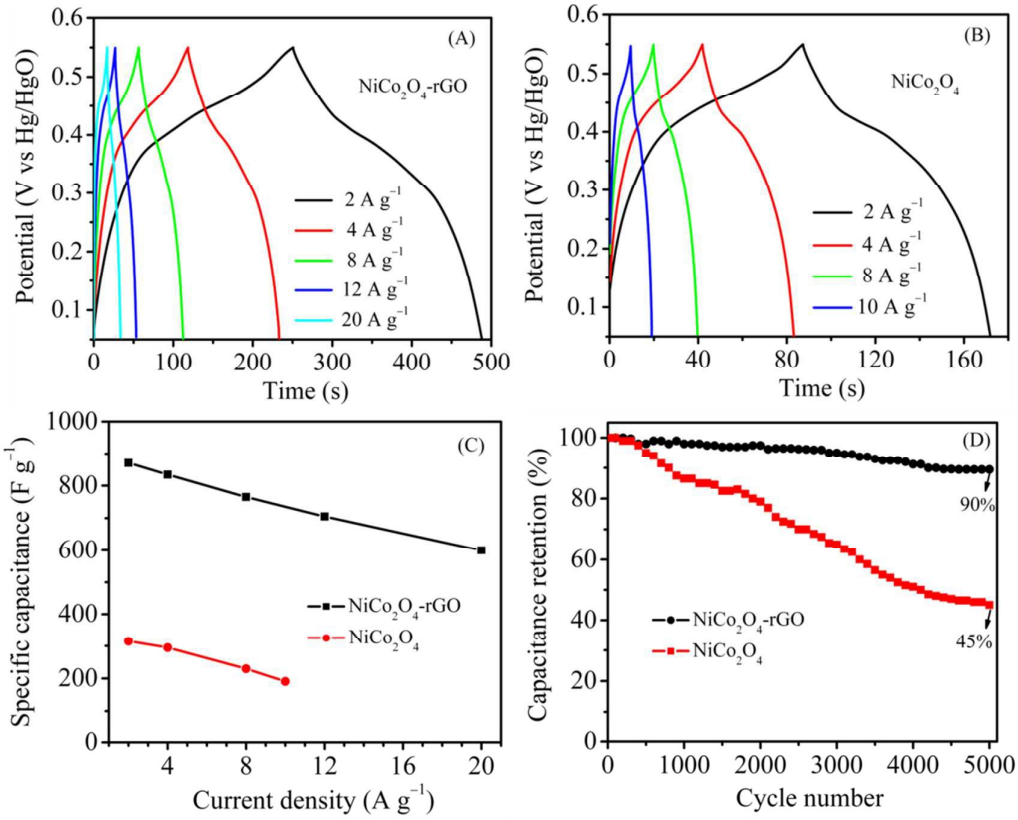

Fig. 9 Charge-discharge curves of (A) $NiCo_2O_4$-rGO and (B) $NiCo_2O_4$ electrodes at different current densities; (C) comparison of current density dependence on specific capacitance values of $NiCo_2O_4$-rGO and $NiCo_2O_4$ electrodes; and (D) capacitance retention of $NiCo_2O_4$-rGO and $NiCo_2O_4$ electrodes as a function of cycle number.

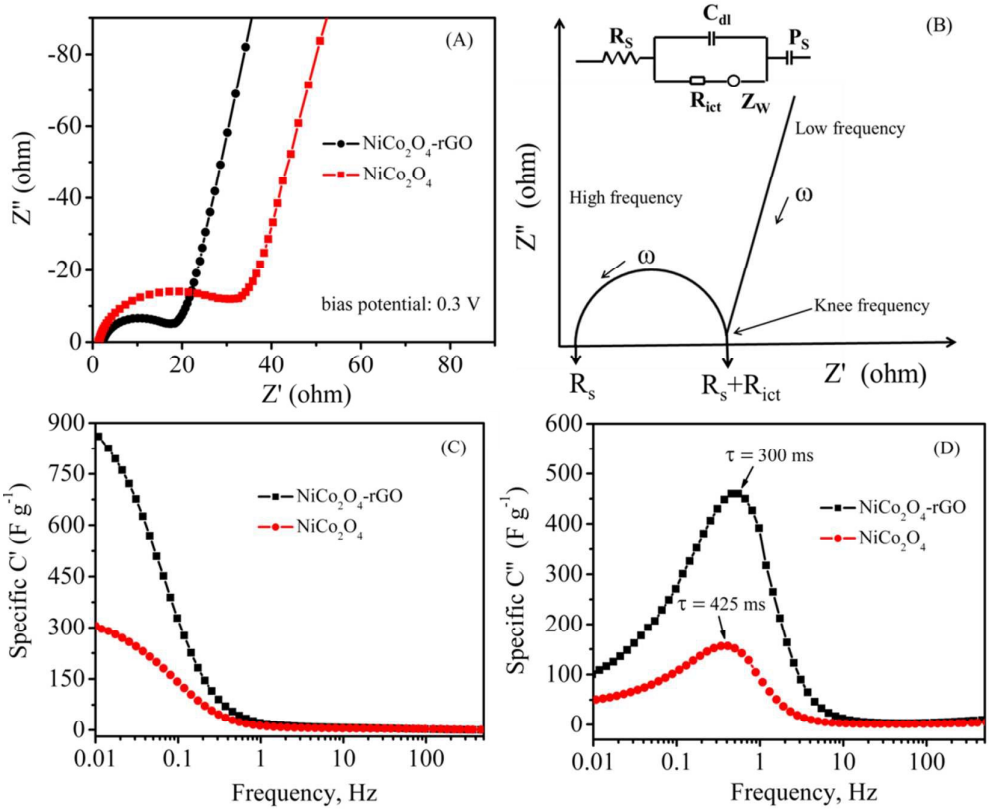

Fig. 10 (A) Complex plane impedance plots (Nyquist plots) of $NiCo_2O_4$-rGO and $NiCo_2O_4$ electrodes at bias potential of 0.3 V, (B) the equivalent circuit of the corresponding electrodes; The variation of the real (C), and imaginary (D) part of specific capacitance with frequency for $NiCo_2O_4$-rGO and $NiCo_2O_4$ electrodes.

Scheme 1. Plausible formation mechanism of ultrathin mesoporous $NiCo_2O_4$-rGO sheets

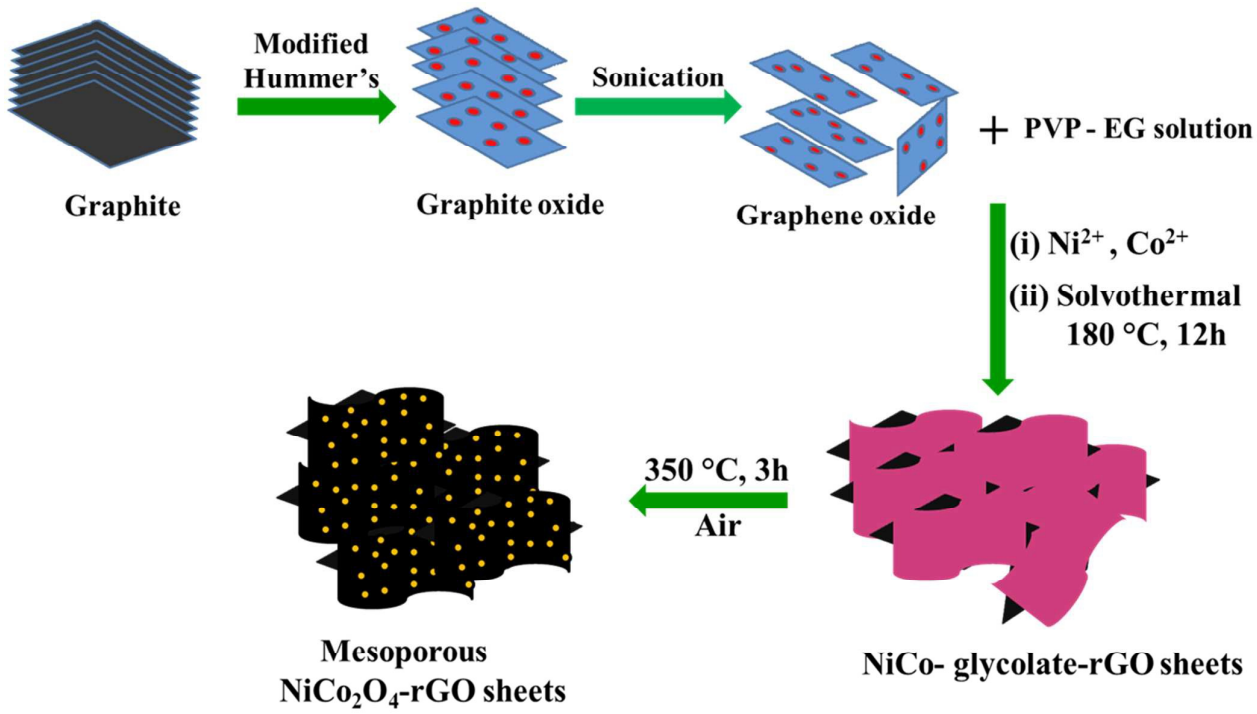

Table 1. Comparison of the electrochemical performance of $NiCo_2O_4$-rGO composite with the literature reports.

Synthesis method	Electrode material	$^{\#}C_S$ (F g^{-1})	*Cyclic performance	Ref.
Solvothermal (PVP surfactant)	$NiCo_2O_4$-rGO	870@2 A g^{-1}	90% after 5000 at 4 A g^{-1}	This work
Electrodeposition	$NiCo_2O_4$/graphene	1078@1mA	60% after 1000 at 3 mA	24
Hydrothermal	RGO-$NiCoO_2$	676@5 mV s^{-1}	No data	36
Hydrothermal	$NiCo_2O_4$@RGO	737@1 A g^{-1}	94% after 3000 at 4 A g^{-1}	38
Microwave	$NiCo_2O_4$@GO	925@1.5 A g^{-1}	94% after 700 at 16 A g^{-1}	39
Sol-gel method	Graphene/NiO	628@1 A g^{-1}	82% after 1000 at 1 A g^{-1}	47
Hydrothermal	Co_3O_4/GNS	157.7@0.1 A g^{-1}	70% after 4000 at 0.2 A g^{-1}	55
Hydrothermal	NRGO-$NiCoO_2$	508@0.5 A g^{-1}	93% after 2000 at 2 A g^{-1}	56
Reflux method	$NiCo_2O_4$ /rGO	1186 @0.5 A g^{-1}	97% after 100 at 0.5 A g^{-1}	57
Electrochemical deposition	$NiCo_2O_4$/CNT	694@1 A g^{-1}	91% after 1500 at 4 A g^{-1}	58

$^{\#}C_S$: maximum specific capacitance obtained from CV or CP test in F g^{-1}.

*Capacitance retention (%) measured by CP test at a specified current density.